



# Computational Design of Three-Dimensional Multi-Constituent Material Microstructure Sets with Prescribed Statistical Constituent and Geometric Attributes

Yaochi Wei<sup>1</sup> · Daniel H. Olsen<sup>1</sup> · Christopher M. Miller<sup>1</sup> · Karla B. Wagner<sup>2</sup> · Amirreza Keyhani<sup>1</sup> · Naresh Thadhani<sup>1,2</sup> · Min Zhou<sup>1,2</sup>

Received: 23 November 2019 / Revised: 17 January 2020 / Accepted: 8 February 2020 / Published online: 24 February 2020

© Korean Multi-Scale Mechanics (KMSM) 2020

## Abstract

The generation of three-dimensional (3D) microstructures with multiple constituents is an important part of multiscale computational simulation and design for a wide range of materials including heterogeneous polycrystalline metals, ceramics, composites, and energetics. Realistic 3D microstructures for multiphase materials are difficult to obtain experimentally or computationally. Challenges include generation and representation of complex constituent morphologies, topological arrangement and distribution, defect description, and statistical conformity. Here, we present a novel technique for systematically composing complex 3D statistically equivalent microstructure sample sets (SEMSS) with prescribed statistical constituents and morphological attributes. Based on large libraries of varying representations of individual constituents, the technique can be used with experimental micro computerized tomography (CT) scans to establish SEMSS that track the attributes of existing materials as well as to design SEMSS for new materials not yet in existence for computational exploration. Heterogeneous systems involving different combinations of molecular crystallites, metallic particles, oxidizer granules, and a polymeric matrix are designed and generated to track the properties of an existing material. The corresponding SEMSS are used in multiphysics simulations accounting for coupled thermal–mechanical processes or thermal–mechanical–chemically reactive processes. The results are used to quantify microstructure-induced response variations and point out the limitations of two-dimensional (2D) microstructures that are direct sections of the full 3D microstructures. The use of the SEMSS has also enabled uncertainty quantification (UQ) and the development of probabilistic characterizations for variations in macroscopic responses due to intrinsic material microstructural heterogeneities.

**Keywords** 3D microstructure · Statistically equivalent microstructures · Geometric attributes · Microstructure design · Uncertainty quantification

## Introduction

The behavior of materials significantly depends on their heterogeneous microstructures [1–3]. In order to develop new materials and improve existing materials for various

applications, it is important to understand and quantify the role of microstructural heterogeneities such as constituent fractions, crystal shape and size, interfaces, and defect content. As such, models that explicitly resolve microstructures and microstructure processes are used. Many models are two-dimensional (2D) and three-dimensional (3D) models are increasingly used. In practice, there are two ways to experimentally obtain 3D microstructure samples. The first is serial sectioning, a destructive characterization tool that involves cropping, polishing, mounting, and optical microscopy [4–7]. The second is non-destructive X-ray computerized tomography (CT) [8–14]. Both methods can be costly, time intensive, and limited in resolution. In addition, separation/identification of different constituents, quantification, and control of microstructural heterogeneities in material

---

Yaochi Wei and Daniel H. Olsen contributed equally to this work.

✉ Min Zhou  
min.zhou@gatech.edu

<sup>1</sup> The George W. Woodruff School of Mechanical Engineering, Georgia Institute of Technology, Atlanta, GA 30332-0405, USA

<sup>2</sup> School of Materials Science and Engineering, Georgia Institute of Technology, Atlanta, GA 30332, USA

preparation are challenges. The resolution and measurement of defects such as interstitials, voids, and cracks are also difficult [15, 16]. These techniques can only allow existing materials to be analyzed and do not lend themselves to exploration and design of new materials.

Compared with the experimental methods, computational generations have advantages: resolution is only limited by computing power and storage, systematic design allows microstructure attributes to be achieved according to prescribed criteria, including the statistical distributions of attributes of individual samples and statistically equivalent microstructure sample sets (SEMSS) that conform to prescribed requirement. SEMSS in simulations are the equivalent of multiple statistically equivalent specimens for the same materials used in experiments to establish statistical variations and probabilistic distributions of material behavior [17]. The statistical variations of macroscopic material behavior due to fundamental material heterogeneities at the microstructural level give rise to uncertainties in analyses. So far, the need for uncertainty quantification (UQ) has not been systematically addressed in many physics-based simulations. The use of SEMSS provides an important avenue to address this need and the concept has mostly been used in 2D simulations [3, 18–30] over the past decade.

Computational design and analyses can also allow material configurations not yet in existence to be explored, thereby providing guidance for materials development. The advent and maturation of additive manufacturing (3D printing) make 3D computational design of materials more important than before.

Computational generation of 3D microstructures has its own challenges which include the creation of realistic constituent morphologies, desired size distributions, proper topological arrangement of constituents, and the detection of overlap of constituents to avoid topologically unrealistic configurations. Lavergne et al. [31] used random sequential adsorption (RSA) [32] to insert polyhedral inclusions to generate representation of the microstructure of a concrete material. Kaeshammer et al. [9] created a library based on CT-scanned RDX (1,3,5-trinitroperhydro-1,3,5-triazine) molecular crystallite grains and used RSA to insert the grains to generate microstructures. Each grain is characterized using several descriptors. To obtain microstructures with desired topological attributes, grains with descriptors within the range of interest are chosen from the library. The microstructures produced involved a population of grains/particles and a matrix, with the grain volume fractions up to ~60%.

In this paper, we present a novel technique for designing 3D microstructures for more realistic representations of different materials. The objective is to enable the generation of (1) microstructures with multiple types of constituents, (2) microstructures with defects such as cracks and voids, (3)

microstructures with solid constituent fractions up to ~80%, and (4) microstructure sample sets with statistically equivalent attributes that conform to prescribed requirements or that match the attributes of experimentally obtained samples. Our approaches are 3D experimental micro CT scans for quantification to guide the computational design, generation of libraries of constituents, composition of microstructures by insertion of selected constituents whose sizes conform to specific statistical distributions, and creation of defects when applicable. A contact algorithm is developed to ensure no interpenetration of constituents and proper constituent topological relations. The techniques are used to create SEMSS for materials with up to four different constituents (crystalline grains, oxidizer crystal granules, metallic particles, and matrix) with and without defects. Simulations are carried out with some of the SEMSS generated, allowing the development of probabilistic quantifications of macroscopic behaviors of materials.

We will first discuss the algorithms for processing the images obtained from experimental CT and characterizing the microstructure statistics. Then we will focus on the generation of a SEMSS matching the statistical attributes of scanned specimens, as well as the generation of the multi-constituent microstructures and the introduction of microstructural defects, followed by a few computational examples with a focus on statistical variations of results from a 3D simulation and 2D simulations using 2D cross-sections of the 3D sample. A summary will be given finally.

## Experiment-Guided 3D Microstructure Design

A polymer-molecular crystal composite is used as the model material for experimental scan, characterization, and design. This material is composed of sucrose particles and a polymer matrix. Sucrose has thermal–mechanical properties similar to those of HMX (1,3,5,7-tetranitro-1,3,5,7-tetrazoctane), an energetic crystal used in applications requiring high-rate release of chemical energy. Because of this, sucrose is a commonly used inert mechanical simulant [33–35] in experiments and simulations for thermal–mechanical response analyses. The sample scanned is a rod. Along the length of the sample, the 3D CT scan consists of 5020 cross-sectional images of  $1972 \times 1897$  pixels each at a resolution of  $5 \mu\text{m} \times 5 \mu\text{m}$  per pixel. The central cylindrical part [7.25 mm (1450 pixels) in diameter and 21.9 mm (4374 pixels) in length] of the scanned material as shown in Fig. 1a is used in the analysis. These images are binarized, non-uniformities and imperfections in each constituent phase [36, 37] are removed using the morphological image processing (MIP) [38, 39] technique. An algorithm is developed to identify the particles or grains via pixel connectivity, allowing

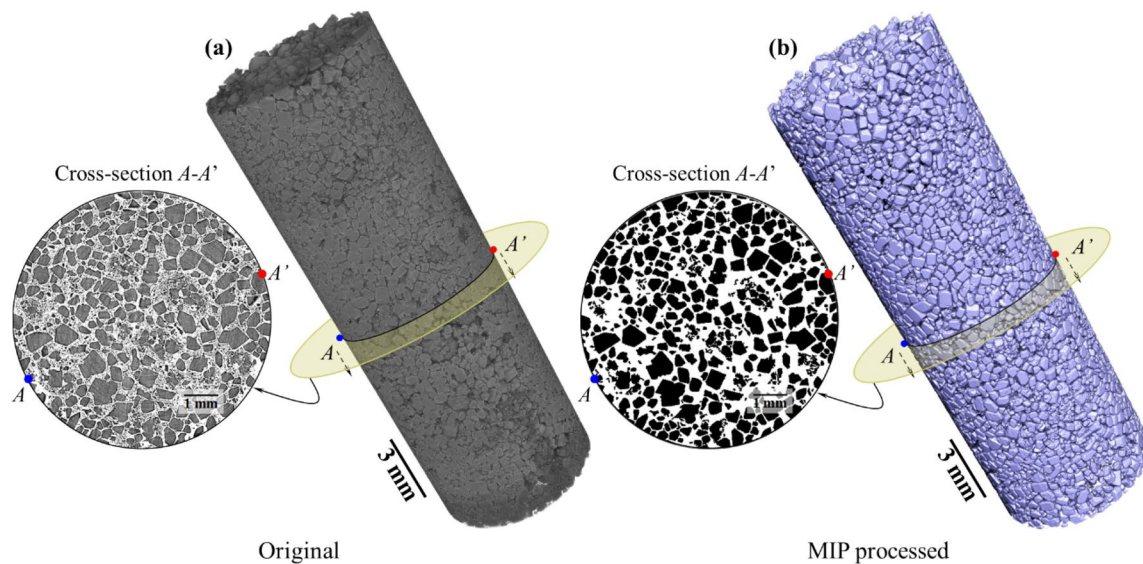


**Fig. 1** 3D microstructure obtained from **a** experimental CT scan and **b** binarization of the scanned images via morphological image processing (MIP). Note that the fuzzy areas in the original image have been removed allowing for the grains underneath to be seen

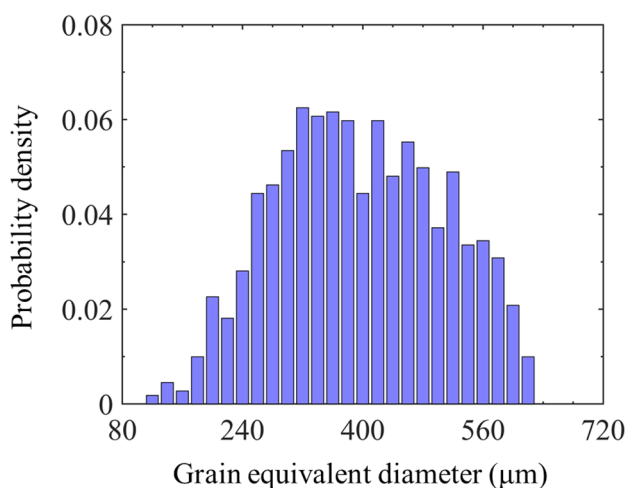


**Fig. 2** Grain size distribution of the experimentally scanned sample. This distribution is used in computational design

statistical quantification of the microstructure to be obtained. The resolution of the process is 20 pixels (100  $\mu\text{m}$ ), as a result particles below this size are not resolved or tracked. It is believed that the volume fraction of the small particles is below 13.4%.

Figure 1 shows both the as-scanned image (Fig. 1a) and the computationally reconstructed image (Fig. 1b). The grain size distribution is shown in Fig. 2. The grain volume fraction is 0.525 and the average equivalent diameter of the grains is 418.8  $\mu\text{m}$  with a standard deviation of 147.0  $\mu\text{m}$ . The crystalline grains are predominantly convex polyhedral in shape.

## Statistically Equivalent Microstructure Sample Sets (SEMSS) with Heterogeneities

### Computationally Generated Microstructure Sample Sets

To characterize the scatter in material behavior and obtain UQ, statistically equivalent microstructure sample sets (SEMSS) with prescribed constituent fractions and size distributions are required. Here, we use the grain distribution in Fig. 2 as a target in the design of a SEMSS. The first step is to establish a library with a wide range of grains which can be used to compose microstructures. To this effect, the 3D Voronoi tessellation [40, 41] is used. The resulting library contains grains with random convex polyhedral shapes representative of the shape of crystallites. This technique yields polycrystalline microstructures whose attributes such as grain size and size distribution can be controlled by the number and location distribution of the seeding sites. The grains in these polycrystalline microstructures are separated at individual geometric objects, categorized, and placed in a library. For this paper, the library contains 600,000 grains and is established using 20 polycrystalline microstructures. Larger libraries can be established when needed.

To compose individual microstructures conforming to a prescribed grain size distribution, grains are randomly picked from the library and checked against the statistical attributes. Those fitting the statistical requirements are used and those not conforming to the requirements are rejected. The accepted grains are randomly placed in a 3D domain whose size is the same as or larger than the size of the

microstructure sample desired. To avoid overlap or interpenetration of different constituents or grains, a contact detection algorithm is developed and used. This algorithm follows each and all vertices of the grains. Each grain is an  $M$ -sided polyhedron with each facet being an  $N$ -sided polygon in 3D. Potential placement of each vertex in all other polyhedrons are checked using its Barycentric coordinates relative to the target grain. If none of the coordinates is negative, indicating the vertex lies within an existing grain, contact or overlap is detected, and the new grain being tested is randomly rotated about its centroid and moved to a random new position. If a grain cannot be placed without contact or overlap after 50 attempts, the grain is discarded and a new grain fitting the requirements is chosen from the library. This process is repeated until the desired fractions of all constituent types are reached.

To illustrate and quantify the statistical variations in microstructure characteristics among the multiple samples in a SEMSS, Fig. 3a shows five cylindrical samples with the same crystalline particle fraction of  $\eta=0.525$  and a matrix fraction of 0.475. The particle size distribution is shown in Fig. 3b, with the solid color line denoting the mean distribution and the error bars denoting the range of variations among all samples in the set. The histogram shows the distribution of the 3D experimentally scanned sample. The computationally generated SEMSS has an average equivalent particle diameter of 418.0  $\mu\text{m}$  and a monomodal size distribution, with a standard deviation of 147.0  $\mu\text{m}$ . As mentioned above, the scanned sample has an average equivalent crystal

diameter of 418.8  $\mu\text{m}$  and a standard deviation of 147.0  $\mu\text{m}$ . Overall, the statistical attributes of the computationally generated SEMSS closely track those of the scanned specimen.

### Microstructure Sample Sets with Geometric Periodicities

Smaller microstructure samples can serve as building blocks to obtain microstructures with larger sizes, providing an efficient means to generate large samples. The process of creating a periodic microstructure includes grain insertion and surface particle cropping. One basic requirement is that the microstructure details on the periodic faces match. To ensure this periodicity of the smaller building block in the particle insertion process, the crystalline granules in the library created are inserted into a cubic domain and the locations to which the particles are assigned have a sequential difference. The specific sequence is: corner, edge, face, and interior with possible duplications. For example, if a particle is to be added to a corner of the domain, the other seven corners of the cubic box are also assigned the same particle (the same point of the eight identical particles occupies the eight corners, see Fig. 4a). Particles on the twelve edges and the six side faces are handled in a similar manner. This ensures a seamlessly stacked structure with all corners, all corresponding edges and all corresponding faces of the cube with coincidental constituent and interfacial feature required for periodicity.

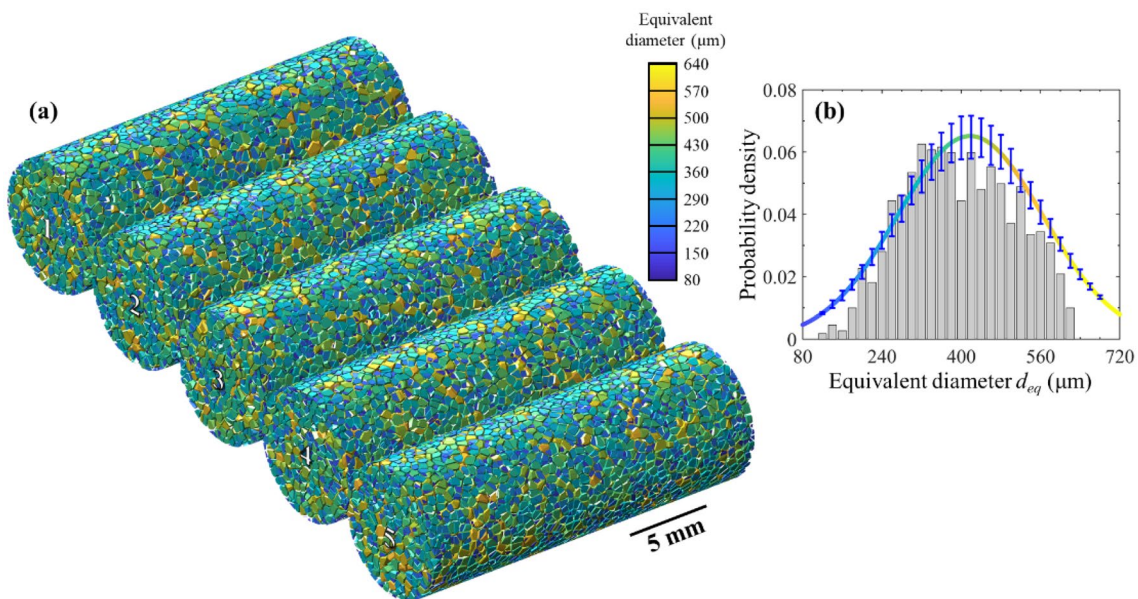


**Fig. 3** Computationally generated 3D cylindrical statistically equivalent microstructure sample set (SEMSS) with a crystalline granule volume fraction of  $\eta = 0.525$ , **a** 3D images of five instantiations, and

**b** granular size distributions. The error bars indicate variations among the samples in the set

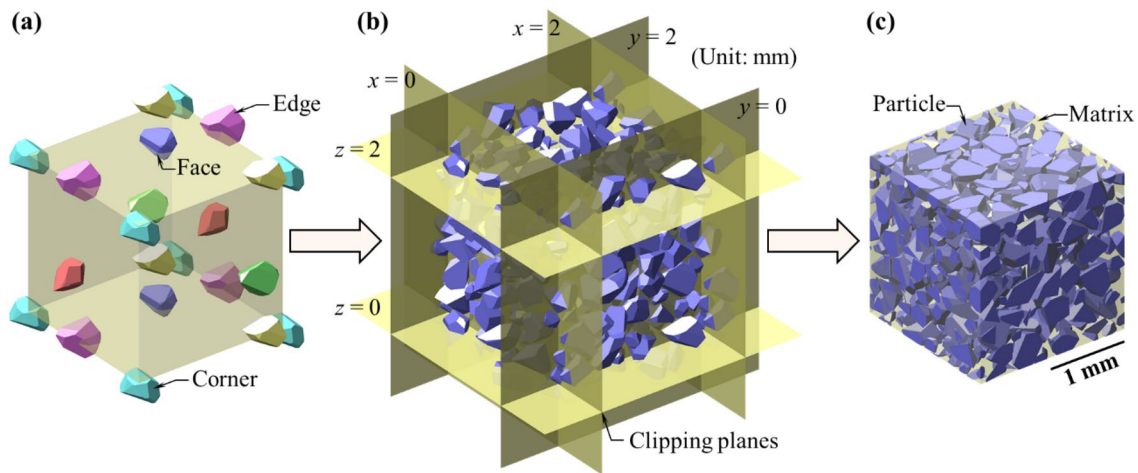


**Fig. 4** Computational generation of a periodic microstructure. **a** Particle insertion on surfaces. Each color represents a group of particles having identical shapes and sizes. **b** The process of surface particle cropping. **c** The periodic structure obtained

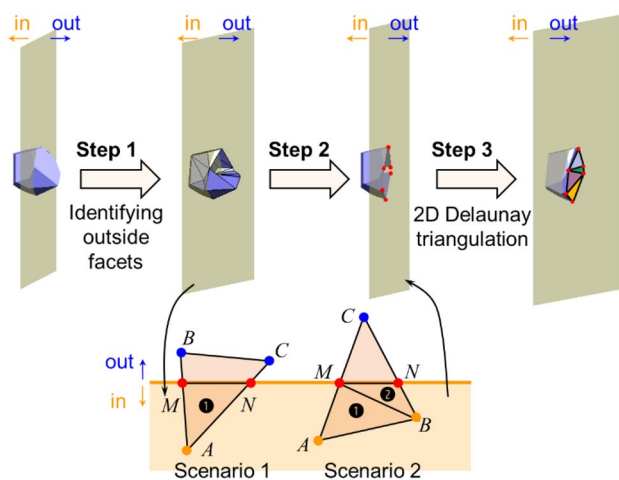


**Fig. 5** Key steps in the cropping algorithm

After the particle insertion is complete, surface particles are clipped by six planes coinciding with the surfaces of the domain box (Fig. 4b) using the cropping algorithm illustrated in Fig. 5. In Step 1 of Fig. 5, all the facets located completely outside the domain are identified and removed. Step 2 involves trimming facets that intersect with the side faces of the cube. A triangular facet  $ABC$  of a particle will have in general two points of intersection on two different linear sides of the triangle. The cropping results in two points  $M$  and  $N$  on the edges. In the two different scenarios illustrated in Fig. 5, the original triangle will be replaced by new triangle(s)  $AMN$  (Scenario 1) or  $ABM$  and  $MBN$  (Scenario 2). After all the intersected triangles are trimmed, 2D Delaunay triangulation [41] is used to create new surfaces of the cropped particle by encompassing all the intersection

points (marked red in Fig. 5). A final periodic microstructure is obtained by closing all the cropped particles (Fig. 4c).

With the building block, microstructures of any larger size can be generated by stitching together building blocks along different directions. Mirroring can also be applied when creating larger microstructures allowing for more variations. Figure 6 shows a SEMSS, each  $6\text{ mm} \times 2\text{ mm} \times 2\text{ mm}$  in size. Each sample contains three building blocks. The granules in this set follow a bimodal size distribution (Fig. 6b).

### Computational Design of Multiple Constituents and/or Defects

It is important to consider full 3D microstructures at the scales of tens of mm, including constituent morphology, multiple constituent distributions, voids, and interfaces, not just individual or small numbers of voids, cracks, or grains. Models at scales of only tens to hundreds of microns, or models not inclusive of realistic and stochastic distributions of all the heterogeneities, are incapable of capturing true and full microstructure effects and uncertainties. For example, some materials (such as polymer-bonded explosives, or PBX) contain not only crystalline grains and polymeric matrix binders, but also oxidizer particles and metallic fuel granules. To generate such microstructures with more than two constituents, creation, identification and insertion of different constituents must be carried out. Figure 7a shows an example microstructure whose constituents include crystalline grains, a polymeric matrix binder, metallic fuel granules, and oxidizer particles. On the other hand, micro defects such as voids, intragranular cracks, and interfacial debonding sites can also be randomly inserted to any prescribed statistical size and location distributions. For example, voids whose sizes follow a certain distribution (Fig. 7c) can be

**Fig. 6** **a** A SEMSS built with cuboid microstructures. Each sample contains three  $2\text{ mm} \times 2\text{ mm} \times 2\text{ mm}$  building blocks. The particle sizes follow a bi-modal distribution as shown in **b**. The error bars indicate variations among the samples in the set

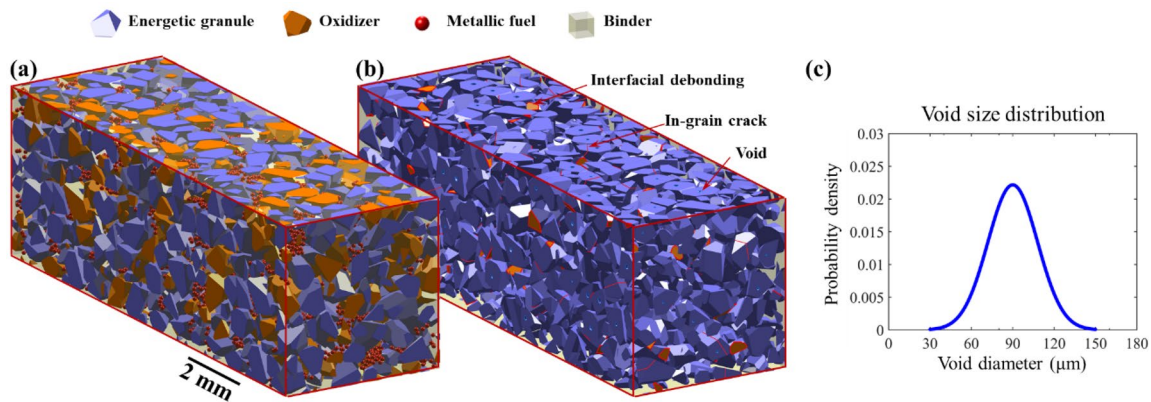
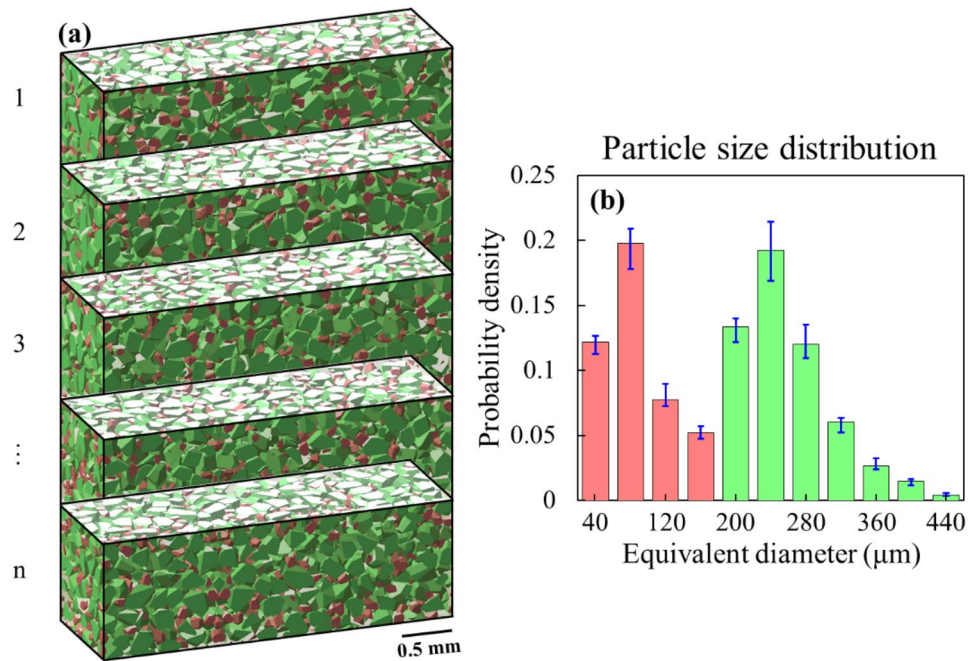


**Fig. 7** Computationally designed microstructures with **a** high-explosive molecular crystalline grains, a polymeric matrix binder, metallic fuel particles, and oxidizer granules, and **b** cracks and voids (conforming to given size distribution in **c**), in addition to different constituents

randomly placed in crystalline grains (Fig. 7b) or other locations. In addition, intragranular and interfacial cracks can also be explicitly resolved in a similar manner (Fig. 7b).

## Computational Applications

During the generation of the 3D microstructures, the constituents and defects are saved in a vectorized format, i.e., the constituents and defects are expressed as individual geometric entities. Specifically, polycrystalline grains, particles, and voids are 3D objects with closed surfaces. These objects are categorized as either solid material (constituents) or empty space (voids). A matrix phase is generated

by filling the space not occupied by the other constituents or voids. The intragranular and interfacial cracks are expressed in terms of flat polygonal surface facets with zero thickness located either within a constituent or between constituents. Because each crack is explicitly stored as an individual geometric entity (flat polygonal facets), its size, shape, and location can be uniquely defined through the parameters of the geometric entity. The sizes, shapes, orientations, and locations of the crack population can be chosen to follow prescribed statistical distributions (e.g., to match distributions in experimentally measured samples). The format allows convenient importation into many meshing tools for discretization before numerical simulations. For implementation in finite element models, meshing can follow the individual

constituents with each element fully within a constituent (typical for Lagrangian approaches) or straddling the boundary of more than one constituent entities (typical for Eulerian approaches). Interfaces and cracks can be easily resolved by using cohesive elements [42–46].

We provide some examples in this section to show the importance of using 3D microstructure models, outline the differences between 3D and 2D models, point out important

techniques introduced above. To ensure that the 2D models are consistent with the 3D model, five evenly spaced 2D cross-sections (slices) of the 3D microstructure in both the  $y$  and  $z$  directions ( $y, z = 0.3, 0.9, 1.5, 2.1,$  and  $2.7$  mm) (Fig. 8b) are also used. A Lagrangian finite element analysis (FEA) is carried out. The governing equations corresponding to the conservation of mass, momentum, and energy are

$$\begin{cases} \det \mathbf{F} = J = \frac{\rho_0}{\rho}, \\ \int_V \boldsymbol{\tau} : \delta \mathbf{D} dV = \int_S \mathbf{t} \cdot \delta \dot{\mathbf{u}} dS + \int_V \rho_0 \mathbf{b} \cdot \delta \dot{\mathbf{u}} dV - \int_V \rho_0 \frac{\partial^2 \mathbf{u}}{\partial t^2} \cdot \delta \dot{\mathbf{u}} dV, \text{ and} \\ \int_V \rho_0 c_p \dot{T} \delta T dV = \int_V \chi_h \boldsymbol{\tau} : \mathbf{D}^p \delta T dV + \int_S k(\mathbf{F}^{-1} \mathbf{F}^{-T} \nabla T) \cdot \mathbf{n} \delta T dS - \int_V k(\mathbf{F}^{-1} \mathbf{F}^{-T} \nabla T) \cdot \nabla \delta T dV. \end{cases} \quad (1)$$

issues that must be addressed in comparing 2D and 3D models, and illustrate how SEMSS can lead to uncertainty quantification of macroscopic material behavior.

### Thermal–Mechanical Analyses Using a 3D Microstructure and Its 2D Cross-Sections

To study the difference in the predictions of the thermo-mechanical deformation between 2D and 3D models, we consider the 3D model in Fig. 8a generated using the

where  $\mathbf{F}, J, \rho_0, \rho, \boldsymbol{\tau}, \mathbf{D}, \mathbf{D}^p, \mathbf{t}, \mathbf{b}, \mathbf{u}, c_p, T, \chi_h,$  and  $k$  denote deformation gradient, Jacobian, mass density in reference configuration, mass density in current configuration, Cauchy stress, rate of deformation, plastic part of rate of deformation, traction on a surface with normal  $\mathbf{n}$  in reference configuration, body force, displacement, specific heat, temperature, fraction of plastic work converted to heat, and heat conductivity. The framework in detail can be found in Kim et al. [26].

The material used in the simulation is PBX 9501 containing HMX grains and Estane binder. The volume and area

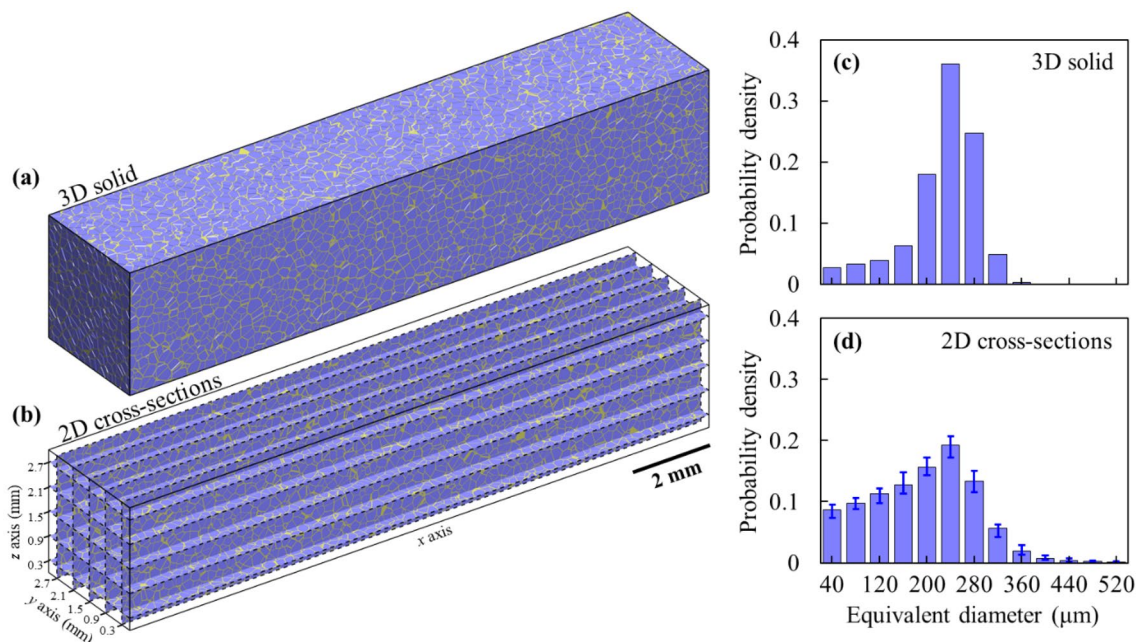


**Fig. 8** **a** A 3D microstructure and **b** ten 2D microstructures obtained from the cross-sections of the 3D microstructure at  $y=0.3, 0.9, 1.5, 2.1,$  and  $2.7$  mm and  $z=0.3, 0.9, 1.5, 2.1,$  and  $2.7$  mm. **c** Particle size

distribution of **a**, **d** particle size distribution of **b**. The error bars indicate variations among the cross-sections

**Table 1** Grain volume/area fractions of the 3D microstructure and its 2D cross-sections

Grain area fractions of 2D cross-sections	Grain volume fraction of 3D microstructure		
y=0.3 mm	0.8034		
y=0.9 mm	0.8021		
y=1.5 mm	0.8078		
y=2.1 mm	0.8040		
y=2.7 mm	0.8029		
z=0.3 mm	0.7987	0.8036	
z=0.9 mm	0.8022		
z=1.5 mm	0.8082		
z=2.1 mm	0.8032		
z=2.7 mm	0.8054		
Mean of 2D	0.8038		

fractions of the HMX grains for the 3D microstructure and its 2D slices are listed in Table 1. The mean of the grain area fractions of the ten cross-sections is close to the grain volume fraction in 3D. The grain material follows a viscoplasticity model that was calibrated based on Zhou et al. [47]. The binder material follows the viscoelasticity model of Mas et al. [48]. Properties and parameters used for the grain and the binder are given in Kim et al. [26], Wei et al. [3], and Mas et al. [48], as listed in Tables 2 and 3.

For both 2D and 3D, the dynamic loading is effected by an imposed piston velocity of  $U_p = 200$  m/s at one end. The conditions of plane strain prevail in the 2D cases. The temperature fields at  $t = 25$  and  $40 \mu\text{s}$  after the onset of loading are shown in Fig. 9a, d for 3D microstructure and Fig. 9b, e for 2D. Figure 9c, f shows the profiles of temperature increases along the longitudinal direction at  $t = 25$  and  $40 \mu\text{s}$ , respectively.

At  $t = 25 \mu\text{s}$  (Fig. 9c), the average temperature rise in 2D cross-sections is approximately 9.3% lower than that in 3D. This percentage difference decreases to 7.1% later at  $t = 40 \mu\text{s}$ . The discrepancies in the temperature rise between the 2D and 3D simulations are purely due to the dimensionality of the models, as all other aspects (governing equations, constitutive descriptions, material parameters, and load intensity) are identical. The likely explanation for this

**Table 2** Parameters in viscoplasticity model of HMX from Kim et al. [26]

$\sigma_0$ (MPa)	$\epsilon_0$	$N$	$T_0$ (K)	$\beta$
260	$5.88 \times 10^{-4}$	0.0	293	0.0
$\dot{\epsilon}_0$ (s <sup>-1</sup> )	$m$	$\dot{\epsilon}_m$ (s <sup>-1</sup> )	$a$ (1/MPa)	$\kappa$
$1 \times 10^{-4}$	100.0	$8.0 \times 10^{12}$	22.5	0.0

difference is that the 2D plane strain formulation limits the degrees of freedom for the overall deformation relative to the full 3D formulation, thereby limiting the overall dissipation that leads to inelasticity induced temperature increase. This analysis provides an important view on the limitation of 2D models.

It is worthwhile to note that, while 2D cross-sections are often regarded and used as representations of the 3D material microstructures [49, 50], some characteristic parameters measured in 2D are different but statistically related to the corresponding parameters in 3D. A case in point is the average size of grains or particles. Here, we take the average diameter of a sparsely distributed and uniform population of spherical particles in 3D as an example. Ashby [51] and Underwood [52] proved that the 1D, 2D, and 3D average diameters are related through

$$f = N_l \cdot d_1 = N_l \cdot \sqrt{\frac{2}{3}} d_2 = N_l \cdot \frac{2}{3} d_3, \tag{2}$$

where  $f$  is the volume fraction of the particles (inclusions),  $N_l$  is the number of intersections a random test line of unit length makes with the particles,  $d_1$  is the mean particle intercept length along the linear test line,  $d_2$  is the mean 2D particle diameter on a random cross-section, and  $d_3$  is the 3D particle diameter [53]. Indeed, 2D sections can be incomplete and misleading representations of 3D microstructures. For example, inconsistency in volume/area fractions and size distributions can exist [54]. In the present paper, while the 3D volume fraction and the 2D area fraction are essentially the same, the average grain size (equivalent diameter) is  $d_2 = 194.2 \mu\text{m}$  for 2D and  $d_3 = 221.0 \mu\text{m}$  for 3D, which approximately conforms to the relation in Eq. (2). Grain size distributions of 3D and 2D microstructures are compared in Fig. 8c, d.

**Table 3** Parameters of Prony series for Estane binder from Mas et al. [48]

Frequency (Hz)	$G_i$ (MPa)	Frequency (Hz)	$G_i$ (MPa)
$10^{-6}$	0.00417	$10^5$	2.6182
$10^{-5}$	0.00741	$10^6$	12.882
$10^{-4}$	0.01585	$10^7$	52.481
$10^{-3}$	0.03802	$10^8$	223.87
$10^{-2}$	0.06761	$10^9$	436.52
$10^{-1}$	0.08913	$10^{10}$	457.09
1	0.1156	$10^{11}$	346.74
$10^1$	0.1422	$10^{12}$	251.19
$10^2$	0.1622	$10^{13}$	177.83
$10^3$	0.2218	$10^{14}$	117.49
$10^4$	0.4753	$10^{15}$	75.858

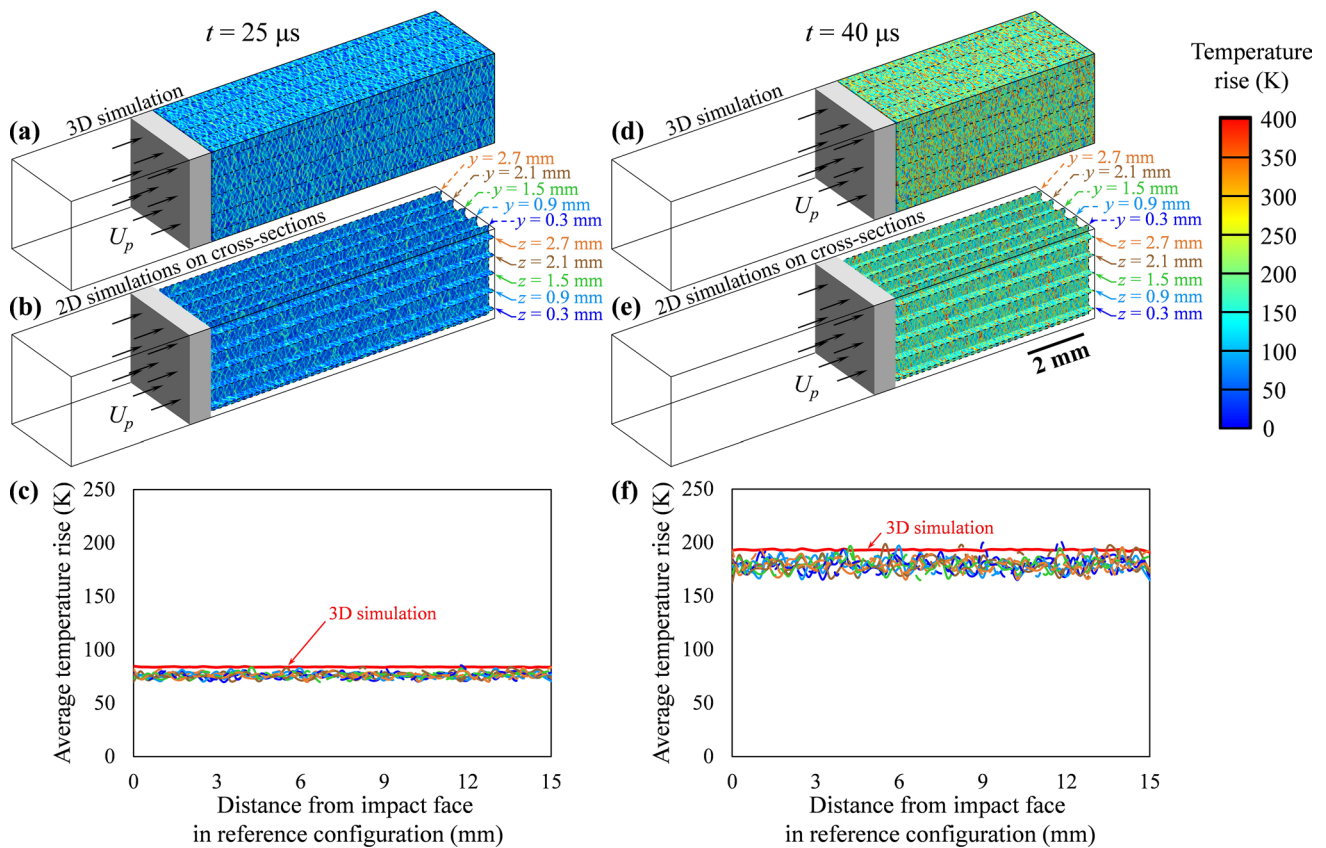


**Fig. 9** Comparison of the temperature distributions obtained from impact simulations using 2D and 3D microstructure samples. The results for  $t = 25 \mu\text{s}$  after onset of loading are: **a** temperature distribution in the 3D microstructure in Fig. 8, **b** temperature distributions in the ten 2D microstructures obtained from the cross sections of the 3D microstructure, and **c** temperature increases along the longitudinal direction of the samples. The results for  $t = 40 \mu\text{s}$  after onset of

loading are: **d** temperature distribution in the 3D microstructure, **e** temperature distributions in the ten 2D microstructures, and **f** temperature increases along the longitudinal direction of the samples. The dynamic loading is effected by an imposed piston velocity of  $U_p = 200 \text{ m/s}$  at one end. In **c**, **f**, the color lines represent profiles for the 2D cross-sections identified in **b**, **d**

### Hotspot Intensity Fields on a 3D Microstructure Under Impact

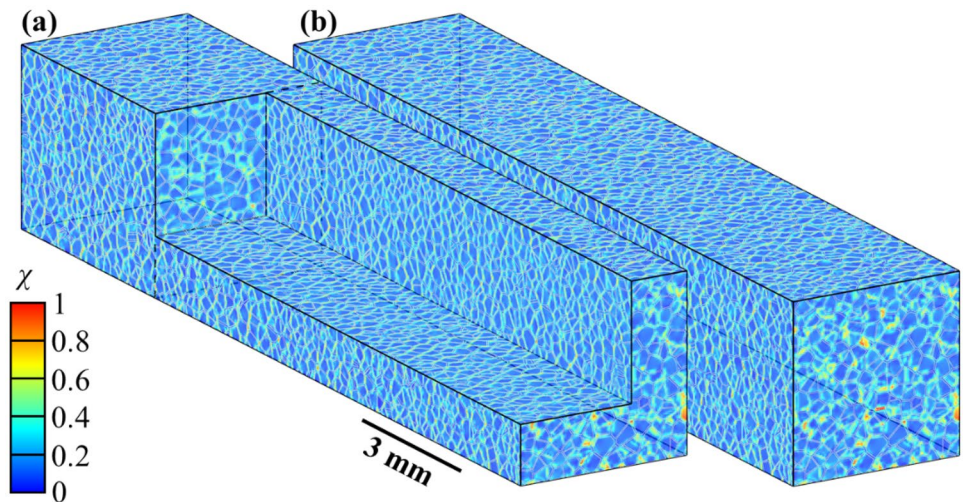
The development of local areas of elevated temperatures in materials under dynamic loading is a concern. This is the case for energetic materials, in which such local areas with elevated temperatures (called hotspots) can lead to the onset of chemical reactions. To quantify the severity of the localized heating, Wei et al. [17] defined the hotspot intensity

$$\chi = \frac{T - T_{\text{ref}}}{T_{\text{max}} - T_{\text{ref}}}, \tag{3}$$

where  $T$  is the local temperature,  $T_{\text{max}}$  is the highest temperature in the whole microstructure under a given condition, and  $T_{\text{ref}}$  is a reference temperature, which is usually

taken as the initial temperature (300 K). The value of  $\chi$  ranges from 0 to 1 and represents the relative strengths of heterogeneous heating in a microstructure that reflect the aggregate effects of microstructure, constituent behavior, deformation/dissipation mechanisms, and loading. It has been shown that the hotspot intensity field in a 3D sample under monotonic impact loading is largely consistent under different load intensities throughout the deformation [17]. The hotspot intensity field can be used as a surrogate for microstructure to approximate the aggregate effects of material heterogeneities on heating in an Eulerian model for reaction initiation, reaction propagation, and shock-to-detonation transition (SDT). Figure 10 shows a hotspot intensity field obtained for a microstructure under monotonic impact velocity  $U_p = 200 \text{ m/s}$ .

**Fig. 10** Hotspot intensity field under monotonic impact velocity  $U_p = 200$  m/s. **a** A cross-sectional view of the whole microstructure **(b)**



### 3D Shock-to-Detonation Sensitivity Analysis with Microstructure Defects and Uncertainty Quantification (UQ)

It is known that micro voids play a very important role in determining the SDT response of energetic materials [55]. However, macroscale simulations with explicit account of voids have been rare or non-existent. Here, we provide an example of how a 3D SEMSS designed using our technique can allow macroscale microstructure-explicit (ME) and void-explicit (VE) simulations to be carried out and lead to the prediction of a macroscopic SDT threshold with uncertainty quantification (UQ) for the first time. The simulations are performed using CTH [56], a multi-material, multi-physics, Eulerian platform that explicitly resolves the coupled thermal–mechanical–chemical processes in an energetic material. The SEMSS designed and used have HMX-based microstructures and an overall macroscale size

of  $15\text{ mm} \times 3\text{ mm} \times 3\text{ mm}$ . Spherical voids with a diameter of  $50\text{ }\mu\text{m}$  are randomly placed in the grains. In Fig. 11a, the total void volume fraction is 10% of the total volume of the material, therefore, there are 206,265 voids in each sample. Dynamic loading is applied through a thick aluminum flyer with a velocity of  $U_p = 600$  m/s. The induced shock pressure is  $P_s = 6.5$  GPa. The SDT analysis (Fig. 11b) shows that under the same shock pressure, the run-to-detonation distance (i.e., the distance which the initial mechanical shock wave has to traverse before becoming a faster, fully chemically active detonation wave front propagating into the virgin, undisturbed material) is longer for the material without voids than that for the material with voids. This distance as a function of applied shock pressure (called Pop plot) is a well-established macroscopic measure of the SDT threshold of energetic materials. Such 3D SEMSS have been used by Miller et al. [55] to predict the macroscopic SDT threshold as functions of microstructure and void attributes. This is

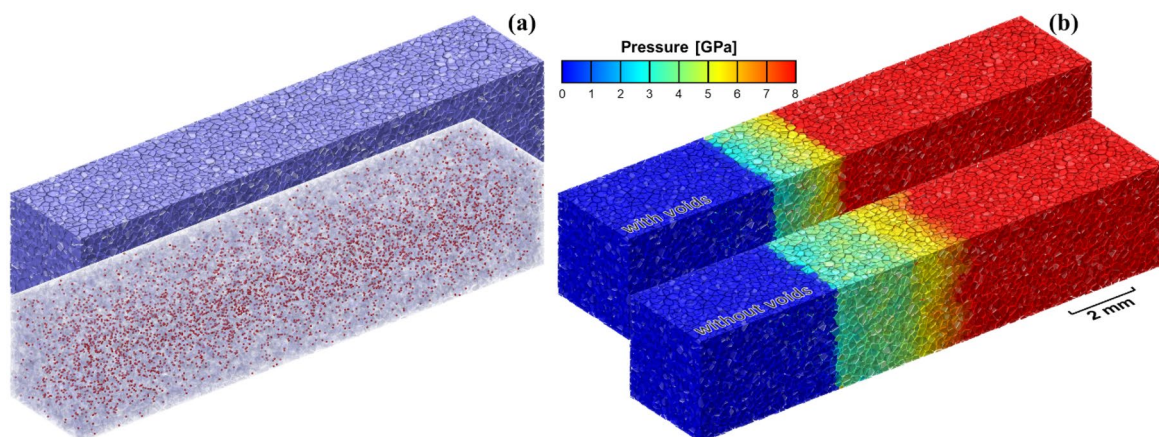


**Fig. 11** **a** HMX-based microstructure with and without voids (5% of the voids are shown for visual clarity) and **b** SDT process of **a** under shock loading of materials with and without voids

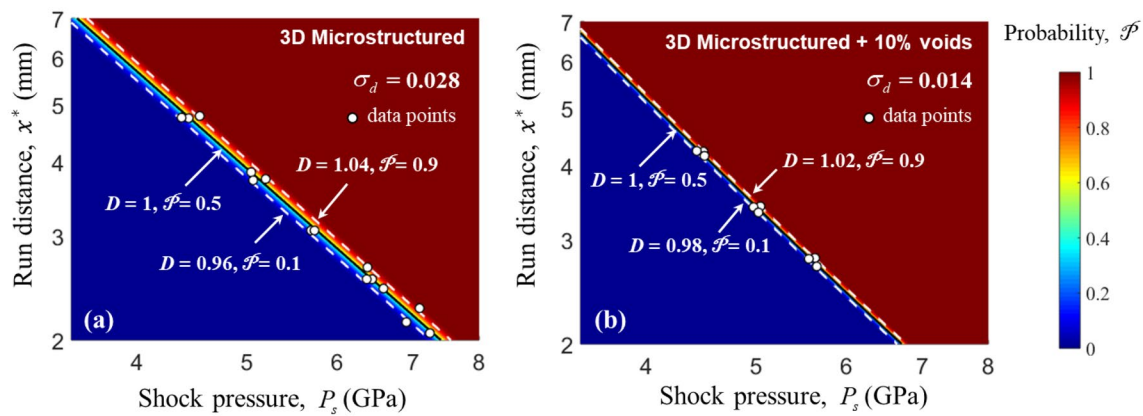


**Fig. 12** Probability distribution maps displaying the likelihood of observing the SDT for a given shock pressure and run distance. Two material cases are shown here: **a** microstructures without voids and **b**

microstructures with 10% voids by volume. The data points for samples in the SEMSS are denoted by white circles. The UQ is carried out using a probabilistic formulation

the first time such a 3D simulation has been carried out at the mm size scale, as far as we are aware of. The simulation captures the process of void collapse and the subsequent heat generation due to plastic dissipation and chemical reaction. Statistical distribution of the macroscopic behavior due to intrinsic microstructural variations in the SEMSS is quantified, allowing the development of a novel probabilistic relation for the SDT threshold. An example is shown in Fig. 12. In this figure, the individual data points from the samples in the SEMSS are shown as white circles.

The statistical scatter in the data points allows quantification of the variations and uncertainties in the macroscale detonation behavior of the material due to intrinsic material heterogeneity variations among samples in the SEMSS. Using a dimensionality reduction parameter  $D$  called the Pop plot number [17] shown in the figure, a probabilistic formulation can be developed. When  $D = 1$ , a data point falls exactly on the Pop plot mean line for a 50% probability of SDT at a given distance and pressure combination. When  $D < 1$  or  $D > 1$ , the data point falls below or above the 50% line, respectively. The probability distribution for UQ analyses in the entire distance-pressure space is [55]

presented in this paper can allow the multiphysics ME and VE simulations, prediction of microscopic behaviors, and probabilistic UQ are given in Refs. [3, 17, 29, 55].

### Conclusions

It is important to carry out full 3D microstructure-explicit and defect-explicit simulations to resolve fundamental multiphysics processes in materials. It is also important to quantify uncertainties in material behavior arising out of intrinsic variations in material microscopic heterogeneities. To enable such analyses, large numbers of 3D microstructure samples are needed. A novel technique for the computational design of 3D statistically equivalent microstructure sample sets (SEMSS) of heterogeneous composite materials is developed. The method uses experimentally-scanned images of actual materials as a statistical guide. To obtain statistical measures of the scanned samples, morphological image processing (MIP) is used to identify the characteristics of the constituents in the samples and establish a library of realistic grain shapes. The size distributions of the constituents can

$$\mathcal{P}(P_s, x^*) = \frac{1}{2} + \frac{1}{2} \operatorname{erf} \left[ \frac{1}{\sqrt{2}\sigma_d} \left( \ln \left( (P_s - P_0)^m \right) + \ln(x^* - x_0^*) - \ln H \right) \right], \tag{4}$$

where  $H$  is a material-dependent scaling parameter,  $m$  is a material-dependent exponent,  $x^*$  is the run-to-detonation distance,  $P_s$  is the shock pressure, and  $\sigma_d$  is the standard deviation of the data about the Pop plot line.  $P_0$  is the shock pressure below which no SDT occurs, and  $x_0^*$  is the theoretical minimum run distance for observing SDT. More details on how the 3D and 2D SEMSS designed using the capability

be used to guide the computational generation of SEMSS with large numbers of microstructures that conform to the attributes of the scanned samples or any desired statistical attributes. In addition to the library of scanned constituents, 3D Voronoi tessellation and other techniques can also be used to generate libraries of crystalline granules with convex polyhedral shape following prescribed size distributions. In

this paper, experimental scan and 3D Voronoi tessellation are used to generate constituent libraries with large numbers of individual grains. The libraries are then used to compose SEMSS with different types of constituent combinations via random placement. An algorithm to detect contact and overlap is developed to prevent interpenetration of the constituents. To create samples of desired external shapes such as planar facets or cylindrical surfaces, a cropping algorithm is also developed. To resolve other geometric discontinuities in microstructures, the technique also lends itself to systematic addition of inclusions and defects in the forms of micro cracks and voids.

Several computational examples are given, in which three-dimensional multiphysics simulations are carried out using the SEMSS generated. Corresponding 2D simulations under otherwise identical conditions are also carried out using 2D cross-sections of a 3D sample. It is shown that differences exist between the 2D and 3D results even accounting for the statistical variations at the microstructure level. The differences are attributed to the fact that the 2D model limits the overall deformation modes in the microstructure, and therefore is only an approximation of the 3D deformation. The SEMSS generated with different constituents and defects have also been used in the studies of the detonation behavior of energetic materials, allowing uncertainty quantification (UQ) and leading to the development of probabilistic relations quantifying the macroscopic shock-to-detonation transition (SDT) threshold as function of statistical variations among samples in the SEMSS.

**Acknowledgements** Support by DTRA through project DTRA1-18-1-0004 (Dr. Jeffery Davis) is gratefully acknowledged. Part of the calculations are performed using supercomputers at the AFRL DSRC of the U.S. DoD High Performance Computing Modernization Program.

## References

1. S. Berbenni, V. Favier, M. Berveiller, Impact of the grain size distribution on the yield stress of heterogeneous materials. *Int. J. Plast.* **23**, 114–142 (2007). <https://doi.org/10.1016/j.ijplasma.2006.03.004>
2. C.A. Tang, H. Liu, P.K.K. Lee, Y. Tsui, L.G. Tham, Numerical studies of the influence of microstructure on rock failure in uniaxial compression—Part I: Effect of heterogeneity. *Int. J. Rock Mech. Min.* **37**, 555–569 (2000). [https://doi.org/10.1016/S1365-1609\(99\)00121-5](https://doi.org/10.1016/S1365-1609(99)00121-5)
3. Y. Wei, S. Kim, Y. Horie, M. Zhou, Quantification of probabilistic ignition thresholds of polymer-bonded explosives with microstructure defects. *J. Appl. Phys.* **124**, 165110 (2018). <https://doi.org/10.1063/1.5031845>
4. O. Forsman, Undersökning av rymdstrukturen hos ett kolstå av hypereutektoid sammansättning. *Jernkontorets Ann.* **102**, 1–30 (1918)
5. M. Hillert, *The Formation of Pearlite (Decomposition of Austenite by Diffusional Process)* (Interscience Publishers, New York, 1962)
6. A. Gurumurthy, A.M. Gokhale, A. Godha, M. Gonzales, Montage serial sectioning: some finer aspects of practice. *Metallogr. Microstruct. Anal.* **2**, 364–371 (2013). <https://doi.org/10.1007/s13632-013-0100-x>
7. H. Singh, A.M. Gokhale, Visualization of three-dimensional microstructures. *Mater. Charact.* **54**, 21–29 (2005). <https://doi.org/10.1016/j.matchar.2004.10.002>
8. V.W. Manner, J.D. Yeager, B.M. Patterson, D.J. Walters, J.A. Stull, N.L. Cordes, D.J. Luscher, K.C. Henderson, A.M. Schmalzer, B.C. Tappan, In situ imaging during compression of plastic bonded explosives for damage modeling. *Materials* **10**, 1–14 (2017). <https://doi.org/10.3390/ma10060638>
9. E. Kaeshammer, P. Dokladal, F. Willot, S. Belon, L. Borne, Generation of virtual microstructures of energetic materials based on micro-computed tomography images analysis. Paper presented at 50th International Annual Conference of the Fraunhofer ICT, Karlsruhe, Germany, 2019
10. M. Ben Youssef, F. Lavergne, K. Sab, K. Miled, J. Neji, Upscaling the elastic stiffness of foam concrete as a three-phase composite material. *Cement Concrete Res.* **110**, 13–23 (2018). <https://doi.org/10.1016/j.cemconres.2018.04.021>
11. A. du Plessis, B.J. Olawuyi, W.P. Boshoff, S.G. le Roux, Simple and fast porosity analysis of concrete using X-ray computed tomography. *Mater. Struct.* **49**, 553–562 (2016). <https://doi.org/10.1617/s11527-014-0519-9>
12. W.J.M. Kort-Kamp, N.L. Cordes, A. Ionita, B.B. Glover, A.L.H. Duque, W.L. Perry, B.M. Patterson, D.A.R. Dalvit, D.S. Moore, Microscale electromagnetic heating in heterogeneous energetic materials based on X-ray computed tomography. *Phys. Rev. Appl.* **5**, 044008 (2016). <https://doi.org/10.1103/PhysRevApplied.5.044008>
13. I.F. Cengiz, J.M. Oliveira, R.L. Reis, Micro-CT—a digital 3D microstructural voyage into scaffolds: a systematic review of the reported methods and results. *Biomater. Res.* **22**, 22–26 (2018). <https://doi.org/10.1186/s40824-018-0136-8>
14. V. Cnudde, A. Cwirzen, B. Masschaele, P.J.S. Jacobs, Porosity and microstructure characterization of building stones and concretes. *Eng. Geol.* **103**, 76–83 (2009). <https://doi.org/10.1016/j.enggeo.2008.06.014>
15. R.M. Doherty, D.S. Watt, Relationship between RDX properties and sensitivity. *Propell. Explos. Pyrot.* **33**, 4–13 (2008). <https://doi.org/10.1002/prep.200800201>
16. U. Teipel, *Energetic Materials: Particle Processing and Characterization* (Wiley, Weinheim, 2004)
17. Y. Wei, R. Ranjan, U. Roy, J.H. Shin, Integrated Lagrangian and Eulerian 3D microstructure-explicit simulations for predicting macroscopic probabilistic SDT thresholds of energetic materials. *Comput. Mech.* **64**, 547–561 (2019). <https://doi.org/10.1007/s00466-019-01729-9>
18. J.L. Jordan, E.B. Herbold, G. Sutherland, A. Fraser, J. Borg, D.W. Richards, Shock equation of state of multi-constituent epoxy-metal particulate composites. *J. Appl. Phys.* **109**, 013531 (2011). <https://doi.org/10.1063/1.3531579>
19. A. Barua, S. Kim, Y. Horie, M. Zhou, Prediction of probabilistic ignition behavior of polymer-bonded explosives from microstructural stochasticity. *J. Appl. Phys.* **113**, 184907 (2013). <https://doi.org/10.1063/1.4804251>
20. Y. Li, M. Zhou, Prediction of fracture toughness of ceramic composites as function of microstructure: I. Numerical simulations. *J. Mech. Phys. Solids* **61**, 472–488 (2013). <https://doi.org/10.1016/j.jmps.2012.09.013>
21. Y. Li, M. Zhou, Prediction of fracture toughness of ceramic composites as function of microstructure: II. Analytical model. *J. Mech. Phys. Solids* **61**, 489–503 (2013). <https://doi.org/10.1016/j.jmps.2012.09.011>

22. S. Kim, A. Barua, Y. Horie, M. Zhou, Ignition probability of polymer-bonded explosives accounting for multiple sources of material stochasticity. *J. Appl. Phys.* **115**, 174902 (2014). <https://doi.org/10.1063/1.4874915>
23. S. Kim, Y. Horie, M. Zhou, Ignition desensitization of PBX via aluminization. *Metall. Mater. Trans. A* **46**, 4578–4586 (2015). <https://doi.org/10.1007/s11661-014-2605-6>
24. Y. Li, M. Zhou, Prediction of fracture toughness scatter of composite materials. *Comp. Mater. Sci.* **116**, 44–51 (2016). <https://doi.org/10.1016/j.commatsci.2015.09.061>
25. S. Kim, C. Miller, Y. Horie, C. Molek, E. Welle, M. Zhou, Computational prediction of probabilistic ignition threshold of pressed granular octahydro-1,3,5,7-tetranitro-1,2,3,5-tetrazocine (HMX) under shock loading. *J. Appl. Phys.* **120**, 115902 (2016). <https://doi.org/10.1063/1.4962211>
26. S. Kim, Y. Wei, Y. Horie, M. Zhou, Prediction of shock initiation thresholds and ignition probability of polymer-bonded explosives using mesoscale simulations. *J. Mech. Phys. Solids* **114**, 97–116 (2018). <https://doi.org/10.1016/j.jmps.2018.02.010>
27. U. Roy, S. Kim, C. Miller, Y. Horie, M. Zhou, Computational study of ignition behavior and hotspot dynamics of a potential class of aluminized explosives. *Model. Simul. Mater. Sci.* **26**, 085004 (2018). <https://doi.org/10.1088/1361-651X/aae402>
28. C. Miller, S. Kim, Y. Horie, M. Zhou, Ignition thresholds of aluminized HMX-based polymer-bonded explosives. *AIP Adv.* **9**, 045103 (2019). <https://doi.org/10.1063/1.5052632>
29. C. Miller, D. Kittell, C. Yarrington, M. Zhou, Prediction of probabilistic detonation threshold via millimeter-scale microstructure-explicit and void-explicit simulations. *Propell. Explos. Pyrot.* **45**, 1–17 (2020). <https://doi.org/10.1002/prep.201900214>
30. A. Keyhani, S. Kim, Y. Horie, M. Zhou, Energy dissipation in polymer-bonded explosives with various levels of constituent plasticity and internal friction. *Comp. Mater. Sci.* **159**, 136–149 (2019). <https://doi.org/10.1016/j.commatsci.2018.12.008>
31. F. Lavergne, K. Sab, J. Sanahuja, M. Bornert, C. Toulemonde, Investigation of the effect of aggregates' morphology on concrete creep properties by numerical simulations. *Cement Concrete Res.* **71**, 14–28 (2015). <https://doi.org/10.1016/j.cemconres.2015.01.003>
32. J. Feder, Random sequential adsorption. *J. Theor. Biol.* **87**, 237–254 (1980). [https://doi.org/10.1016/0022-5193\(80\)90358-6](https://doi.org/10.1016/0022-5193(80)90358-6)
33. C.R. Siviour, P.R. Laity, W.G. Proud, J.E. Field, D. Porter, P.D. Church, P. Gould, W. Huntingdon-Thresher, High strain rate properties of a polymer-bonded sugar: their dependence on applied and internal constraints. *Proc. R. Soc. Math. Phys.* **464**, 1229–1255 (2008). <https://doi.org/10.1098/rspa.2007.0214>
34. J.D. Yeager, A.L.H. Duque, M. Shorty, P.R. Bowden, J.A. Stull, Development of inert density mock materials for HMX. *J. Energ. Mater.* **36**, 253–265 (2018). <https://doi.org/10.1080/07370652.2017.1375049>
35. A. Keyhani, R. Yang, M. Zhou, Novel capability for microscale in situ imaging of temperature and deformation fields under dynamic loading. *Exp. Mech.* **59**, 775–790 (2019). <https://doi.org/10.1007/s11340-019-00495-2>
36. D.J. Benson, P. Conley, Eulerian finite-element simulations of experimentally acquired HMX microstructures. *Model. Simul. Mater. Sci. Eng.* **7**, 333–354 (1999). <https://doi.org/10.1088/0965-0393/7/3/304>
37. E.M. Mas, B.E. Clements, A. Ionita, P. Peterson, Finite element method calculations on statistically consistent microstructures of PBX 9501. *AIP Conf. Proc.* **845**, 487–490 (2006). <https://doi.org/10.1063/1.2263366>
38. H. Minkowski, Vorlumen und oberfläche. *Math. Ann.* **57**, 447–495 (1903). <https://doi.org/10.1007/BF01445180>
39. P. Maragos, Tutorial on advances in morphological image-processing and analysis. *Opt. Eng.* **26**, 623–632 (1987). <https://doi.org/10.1117/12.7974127>
40. C.B. Barber, D.P. Dobkin, H. Huhdanpaa, The Quickhull algorithm for convex hulls. *ACM Trans. Math. Softw.* **22**, 469–483 (1996). <https://doi.org/10.1145/235815.235821>
41. A. Okabe, B. Boots, K. Sugihara, S.N. Chiu, D.G. Kendall, *Spatial Tessellations: Concepts and Applications of Voronoi Diagrams* (Wiley, New York, 2000)
42. D.S. Dugdale, Yielding of steel sheets containing slits. *J. Mech. Phys. Solids* **8**, 100–104 (1960). [https://doi.org/10.1016/0022-5096\(60\)90013-2](https://doi.org/10.1016/0022-5096(60)90013-2)
43. A. Needleman, A continuum model for void nucleation by inclusion debonding. *J. Appl. Mech.* **54**, 525–531 (1987). <https://doi.org/10.1115/1.3173064>
44. V. Tvergaard, J.W. Hutchinson, The relation between crack-growth resistance and fracture process parameters in elastic plastic solids. *J. Mech. Phys. Solids* **40**, 1377–1397 (1992). [https://doi.org/10.1016/0022-5096\(92\)90020-3](https://doi.org/10.1016/0022-5096(92)90020-3)
45. G.T. Camacho, M. Ortiz, Computational modelling of impact damage in brittle materials. *Int. J. Solids Struct.* **33**, 2899–2938 (1996). [https://doi.org/10.1016/0020-7683\(95\)00255-3](https://doi.org/10.1016/0020-7683(95)00255-3)
46. J. Zhai, V. Tomar, M. Zhou, Micromechanical simulation of dynamic fracture using the cohesive finite element method. *J. Eng. Mater. Technol.* **126**, 179–191 (2004). <https://doi.org/10.1115/1.1647127>
47. M. Zhou, A. Needleman, R.J. Clifton, Finite-element simulations of shear localization in plate impact. *J. Mech. Phys. Solids* **42**, 423–458 (1994). [https://doi.org/10.1016/0022-5096\(94\)90026-4](https://doi.org/10.1016/0022-5096(94)90026-4)
48. E.M. Mas, B.E. Clements, B. Blumenthal, C.M. Cady, G.T. Gray, C. Liu, A viscoelastic model for PBX binders. *AIP Conf. Proc.* **620**, 661–664 (2002). <https://doi.org/10.1063/1.1483625>
49. P. Zhang, Microstructure generation of asphalt concrete and lattice modeling of its cracking behavior under low temperature. PhD Thesis, North Carolina State University, North Carolina, USA (2004)
50. L. T. de Souza, Investigation of aggregate angularity effects on asphalt concrete mixture performance using experimental and virtual asphalt samples. Master Thesis, University of Nebraska-Lincoln, Nebraska, USA (2009)
51. M.F. Ashby, The hardening of metals by non-deforming particles. *Z. Metallkd.* **55**, 5–17 (1964)
52. E.E. Underwood, *Quantitative Stereology* (Addison-Wesley Educational Publishers Inc., Reading, 1970)
53. M. Zhou, R.J. Clifton, Dynamic ductile rupture under conditions of plane strain. *Int. J. Impact Eng.* **19**, 189–206 (1997). [https://doi.org/10.1016/S0734-743x\(97\)00028-6](https://doi.org/10.1016/S0734-743x(97)00028-6)
54. Y.R. Kim, M. Haft-Javaherian, L.S. Castro, Two-dimensional virtual microstructure generation of particle-reinforced composites. *J. Comput. Civ. Eng.* **30**, 04014112 (2016). [https://doi.org/10.1061/\(Asce\)Cp.1943-5487.0000448](https://doi.org/10.1061/(Asce)Cp.1943-5487.0000448)
55. C. Miller, D. Olsen, Y. Wei, M. Zhou, Three-dimensional microstructure-explicit and void-explicit mesoscale simulations of detonation of HMX at millimeter sample size scale (**under review**) (2020)
56. J.M. Mcglaun, S.L. Thompson, M.G. Elrick, CTH—a three-dimensional shock-wave physics code. *Int. J. Impact Eng.* **10**, 351–360 (1990). [https://doi.org/10.1016/0734-743x\(90\)90071-3](https://doi.org/10.1016/0734-743x(90)90071-3)